Modeling of surface tension and contact angles with smoothed particle hydrodynamics

Alexandre Tartakovsky[1,*] and Paul Meakin[2]

[1]*Pacific Northwest National Laboratory, P.O. Box 999/MS K1-85, Richland, Washington 99352, USA*
[2]*Idaho National Laboratory, P.O. Box 1625, MS 2025, Idaho Falls, Idaho 83415-2025, USA*

A two-dimensional numerical model based on smoothed particle hydrodynamics (SPH) was used to simulate unsaturated (multiphase) flow through fracture junctions. A combination of standard SPH equations with pairwise fluid-fluid and fluid-solid particle-particle interactions allowed surface tension and three-phase contact dynamics to be simulated. The model was validated by calculating the surface tension in four different ways: (i) from small-amplitude oscillations of fluid drops, (ii) from the dependence of the capillary pressure on drop radius, (iii) from capillary rise simulations, and (iv) from the behavior of a fluid drop confined between parallel walls under the influence of gravity. All four simulations led to consistent values for the surface tension. The dependence of receding and advancing contact angles on droplet velocity was studied. Incorporation of surface tension and fluid-solid interactions allowed unsaturated flow through fracture junctions to be realistically simulated, and the simulation results compare well with the laboratory experiments of Dragila and Weisbrod.

I. INTRODUCTION

Multiphase flow in fracture apertures plays an important role in ground water recharge [1], oil recovery [2], and the behavior of hydrothermal systems [3]. Fractures may also strongly decrease the time required for contaminants to migrate through the vadose zone to an underlying aquifer [4]. Computer modeling is playing an ever increasing role in the development of a better understanding of the behavior of fluids in the subsurface. However, the application of standard grid-based numerical methods to multiphase fluid-flow processes with complex dynamical interfaces is fraught with difficulties such as artificial interface broadening and grid entanglement [5]. The complex dynamics of contact angles also complicates the application of grid-based techniques to modeling flow in domains in which fluid-solid interactions play an important role. Consequently lattice Boltzmann simulations [6,7] have been more widely applied to multiphase fluid flow. Some lattice Boltzmann models for multiphase fluid flow violate Galilean invariance [8], but this is more of theoretical interest than practical importance for the low fluid velocity applications described in this work. A disadvantage of smoothed particle hydrodynamics (SPH) models is that their particle nature leads to "artificial" contributions to both the viscosity and surface tension. In addition, in the SPH model presented in this paper, the surface tension is generated primarily by particle-particle interactions, and there is no analytical relationship between these interactions and the surface tension. In lattice Boltzmann models, there is a simple relationship between the kinematic viscosity and the relaxation parameter [6,7], and the surface tension can be calculated directly from the model parameters if the lattice Boltzmann model is based on a Landau-Ginzburg and Cahn-Hilliard type of free energy functional [9]. However, if the

popular particle-particle interaction approach is used [10], the surface tension of the lattice Boltzmann fluid must be measured using approaches like those applied to the SPH model described in this paper. Current applications of lattice Boltzmann simulations to modeling multiphase flows are limited to the density ratio between fluid phases of less than 50 due to stability issues [10]. Inability to handle large density contrasts seriously limits the application of lattice Boltzmann methods to unsaturated flow processes of practical importance. In particular, density ratios of $\approx 1000:1$ and viscosities ratios of $\approx 100:1$ typical of many liquid-air systems at standard temperature and pressure are out of the reach of current lattice Boltzmann models.

An alternative approach to modeling multiphase flow in domains with complex solid boundaries is to use Lagrangian particle-based methods such as SPH or dissipative particle dynamics (DPD). These methods share with lattice Boltzmann simulations the advantage of not requiring explicit interface tracking or contact angle models, and in addition, SPH and DPD fluids are manifestly Galilean invariant and isotropic because particle-particle interactions depend on *relative* particle positions and velocity differences. In particle-based methods, the fluid-fluid interfaces move with the particles, there is no need to explicitly track the fluid-fluid interfaces, and processes such as fluid fragmentation and coalescence can be handled without difficulty. In addition, the particle nature of SPH and DPD models allows fluid-solid interactions to be modeled through simple particle-particle interactions. Dissipative particle dynamics differs from SPH because random particle-particle interactions are included to represent the effects of thermally driven fluctuations [11,12]. The particles in DPD simulations represent only a small cluster of atoms or molecules while SPH was initially developed for astrophysical fluid dynamics where SPH particles represented large fluid volumes. Consequently DPD has been applied primarily to mesoscale (between the molecular and hydrodynamic scales) processes

---

*Electronic address: Alexandre.Tartakovsky@pnl.gov

026301-1

while the application of SPH to small-scale processes, such as fluid flow in fractures and porous media, is a relatively recent development. To simulate hydrodynamic behavior using DPD a very large number of particles may be required (but not as large as the number of particles required in molecular dynamics simulations) to "average away" the effects of the random fluctuations. In SPH simulations, on the other hand, the number of particles needed is determined by the required resolution and accuracy of the numerical solutions.

In this paper we describe a numerical model based on SPH that was developed to simulate multiphase fluid flow through unsaturated fracture apertures. SPH is an interpolation-based method that can be used to numerically solve systems of partial differential equations. The Lagrangian particle nature of SPH allows physical and chemical effects to be incorporated into the modeling of flow processes that may also be complicated by irregular and deformable boundaries. SPH was first introduced by Lucy [13] and by Gingold and Monaghan [14] for the solution of Navier-Stokes equations in the context of astrophysical fluid dynamics. Since its introduction, SPH has been successfully used to model a wide range of fluid flow processes and the behavior of solids subjected to large deformations. For example, Monaghan [15] used SPH to model the collapse of dams, Morris *et al.* [16] extended SPH to model low-Reynolds-number flows, and Zhu *et al.* [17] and Zhu and Fox [18] applied SPH to study pore-scale flow and transport in saturated porous media.

Incorporation of the effects of surface tension into SPH simulations has been a vexing problem. Morris [19] modeled surface tension based on its macroscopic description with surface tension forces that were proportional to the fluid-fluid interface curvature. This approach gives an accurate estimation of the effects of surface tension but involves rather complex calculations of front curvatures that, in some cases, may lead to significant errors. Nugent and Posch [20] used attractive forces, corresponding to the cohesive pressure in the van der Waals equation of state, to simulate surface tension in two-dimensional SPH simulations. They found that it was necessary to increase the range of the attractive forces to at least twice the range of the SPH weighting function to obtain stable liquid drops, a costly solution causing a significant increase in the computer time required to perform a simulation. In the work described in this paper a combination of short-range repulsive and (relatively) long-range attractive particle-particle interactions was used (with the range of the attractive interactions equal to the range of the SPH weighting function) with standard SPH equations. Incorporating particle-particle interaction forces into the SPH model allows us to simulate not only surface tension but also fluid-solid interactions, resulting in well-defined fluid-solid contact angles under both static and dynamic conditions. The use of a combination of short-range repulsive and long-range attractive interactions was motivated by the molecular origins of surface tension. The consistency of the proposed model was verified by estimating the surface tension and contact angles from four different numerical experiments. In addition, numerical simulations of fluid flow through an unsaturated fracture junction were used to illustrate the application of this approach to practical problems, and the simulation results compared well with the laboratory experiments of Dragila and Weisbrod [1].

II. SPH EQUATIONS

In SPH, the fluid is represented by a discrete set of N particles. The position of the ith particle is denoted by the vector $\mathbf{r}_i$, $i=1,\ldots,N$, and each particle has a mass m_i and density ρ_i. The SPH theory is based on the idea that a continuous field $A(\mathbf{r})$ at position $\mathbf{r}$ can be smoothed by a convolution integral:

$$A_s(\mathbf{r}) = \int A(\mathbf{r}')W(\mathbf{r}-\mathbf{r}',h)d\mathbf{r}', \qquad (1)$$

where $A_s(\mathbf{r})$ is the smoothed field and the weighting function W with a range or support scale h satisfies the normalization condition

$$\int W(\mathbf{r}-\mathbf{r}',h)d\mathbf{r}' = 1. \qquad (2)$$

The integration in Eq. (1) is performed over the entire space of the field, and in the $h\to 0$ limit in which W becomes a Dirac delta function, $A_s(\mathbf{r})\to A(\mathbf{r})$.

Properties associated with any particle i are calculated by approximating the integral in Eq. (1) by the sum

$$A_i = \sum_j \Delta V_j A_j W(\mathbf{r}_i-\mathbf{r}_j,h) = \sum_j m_j \frac{A_j}{\rho_j} W(\mathbf{r}_i-\mathbf{r}_j,h), \quad (3)$$

where ΔV_j is the volume occupied by particle j, ρ_j is the density at position $\mathbf{r}_j$, and the gradients of these properties are approximated by

$$\boldsymbol{\nabla} A_i = \sum_j \Delta V_j A_j \boldsymbol{\nabla}_i W(\mathbf{r}_i-\mathbf{r}_j,h) = \sum_j m_j \frac{A_j}{\rho_j} \boldsymbol{\nabla}_i W(\mathbf{r}_i-\mathbf{r}_j,h).$$
$$(4)$$

The magnitude of the field at any position $\mathbf{r}$ is approximated by

$$A(\mathbf{r}) = \sum_j m_j \frac{A_j}{\rho_j} W(\mathbf{r}-\mathbf{r}_j,h), \qquad (5)$$

and the gradient of $A(\mathbf{r})$, $\boldsymbol{\nabla} A(\mathbf{r})$, can be approximated by

$$\boldsymbol{\nabla}_{\mathbf{r}} A(\mathbf{r}) = \sum_j m_j \frac{A_j}{\rho_j} \boldsymbol{\nabla}_{\mathbf{r}} W(\mathbf{r}-\mathbf{r}_j,h), \qquad (6)$$

where the summation is performed over all particles. The density ρ_i can be found from Eq. (3) which becomes

$$\rho_i = \sum_j m_i W(\mathbf{r}_i-\mathbf{r}_j,h) \qquad (7)$$

for $A_i = \rho_i$.

A variety of forms, including spline functions of different order, have been used for the weighting functions. We found that, for an accurate representation of free surfaces, a spline function of at least fourth order is needed, and we used the fourth-order weighting function [9]

$$W(\mathbf{r},h) = \alpha \begin{cases} \left(3 - \dfrac{3|\mathbf{r}|}{h}\right)^5 - 6\left(2 - \dfrac{3|\mathbf{r}|}{h}\right)^5 + 15\left(1 - \dfrac{3|\mathbf{r}|}{h}\right)^5, & 0 \le |\mathbf{r}| < h/3, \\[2mm] \left(3 - \dfrac{3|\mathbf{r}|}{h}\right)^5 - 6\left(2 - \dfrac{3|\mathbf{r}|}{h}\right)^5, & h/3 \le |\mathbf{r}| < 2h/3, \\[2mm] \left(3 - \dfrac{3|\mathbf{r}|}{h}\right)^5, & 2h/3 \le |\mathbf{r}| < h, \\[2mm] 0, & |\mathbf{r}| > h, \end{cases} \tag{8}$$

where $\alpha = 63/478\pi h^2$ in two spatial dimensions.

The motion of each particle is governed by momentum conservation described by the Navier-Stokes equation

$$\frac{d\mathbf{v}_i(t)}{dt} = -\frac{\nabla P_i(t)}{\rho_i} + \frac{\mu_i}{\rho_i}\nabla^2 \mathbf{v}_i(t) + \mathbf{g} \tag{9}$$

and mass conservation represented by

$$\frac{d\rho_i}{dt} = \nabla \cdot (\rho_i \mathbf{v}_i). \tag{10}$$

Using the SPH approximations (3) and (4) for functions and their gradients, an SPH representation of the Navier-Stokes equations can be obtained.

A number of SPH approximations to the Navier-Stokes equation have been described in the literature [21], and the momentum conservation equation

$$\frac{d\mathbf{v}_i}{dt} = -\sum_j m_j \left(\frac{P_j}{\rho_j^2} + \frac{P_i}{\rho_i^2}\right)\nabla_i W(\mathbf{r}_i - \mathbf{r}_j, h)$$
$$+ 2\eta \sum_j m_j \frac{(\mathbf{v}_i - \mathbf{v}_j)}{\rho_i \rho_j (\mathbf{r}_i - \mathbf{r}_j)^2}(\mathbf{r}_i - \mathbf{r}_j) \cdot \nabla_i W(\mathbf{r}_i - \mathbf{r}_j, h) + \mathbf{g}, \tag{11}$$

defined for each particle, was used in the work described in this paper ($\mathbf{v}_i$ is the velocity of the ith particle). In Eq. (11), the SPH representation of the pressure gradient [the first term on the right-hand site of Eq. (11)] was derived by Monaghan [21] and the SPH representation of the viscous force was obtained by Morris *et al.* [16]. Equation (10) determines the evolution of the particle density. For simplicity and exact mass conservation, the density of each particle is commonly computed directly from Eq. (7).

Given the densities ρ_i, the pressures P_i in Eq. (11) are obtained from the equation of state. In this work a van der Waals equation of state was used in which the pressure is given by [20]

$$P = \frac{\rho \bar{k} T}{1 - \rho \bar{c}_1} - \bar{c}_2 \rho^2, \tag{12}$$

where $\bar{k} = k_b/m$ (k_b is the Boltzmann constant), $\bar{c}_1 = c_1/m$, and $\bar{c}_2 = c_2/m$. Here, c_1 and c_2 are the van der Waals constants and m is the mass of the particles.

To simulate the effect of surface tension and fluid solid interactions particle-particle interactions were added in Eq. (11), leading to the particle equation of motion

$$\frac{d\mathbf{v}_i}{dt} = -\sum_j m_j \left(\frac{P_j}{\rho_j^2} + \frac{P_i}{\rho_i^2}\right)\nabla_i W(\mathbf{r}_i - \mathbf{r}_j, h)$$
$$+ 2\eta \sum_j m_j \frac{(\mathbf{v}_i - \mathbf{v}_j)}{\rho_i \rho_j (\mathbf{r}_i - \mathbf{r}_j)^2}(\mathbf{r}_i - \mathbf{r}_j) \cdot \nabla_i W(\mathbf{r}_i - \mathbf{r}_j, h) + \mathbf{g}$$
$$+ \frac{1}{m_i}\mathbf{F}_i, \tag{13}$$

where $\mathbf{F}_i$, is the force acting on particle i due to the particle-particle interactions with interaction forces given by

$$\mathbf{F}_{ij} = \begin{cases} s_{ij} \cos\left(\dfrac{1.5\pi}{3h}|\mathbf{r}_j - \mathbf{r}_i|\right)\dfrac{\mathbf{r}_j - \mathbf{r}_i}{|\mathbf{r}_j - \mathbf{r}_i|}, & |\mathbf{r}_j - \mathbf{r}_i| \le h, \\[2mm] 0, & |\mathbf{r}_j - \mathbf{r}_i| > h, \end{cases} \tag{14}$$

where s_{ij} is the strength of the force acting between particles i and j. The total force due to interparticle interactions acting on any particle i can then be found from

$$\mathbf{F}_i = \sum_j \mathbf{F}_{ij}. \tag{15}$$

Since $\mathbf{F}_{ij} = -\mathbf{F}_{ji}$, the particle-particle interactions conserve momentum. The exact form of the particle-particle interactions is not critical to the success of the simulations, but the interactions should be repulsive at short distances and attractive at large distances. In addition, computational efficiency requires a long-distance cutoff (at h in this case) to reduce the number of particle-particle interactions that must be calculated, and the particle-particle interactions should be "soft" to allow reasonably long time steps to be used. For a given fluid, the magnitude of this force depends only on the distance between particles. The force is repulsive for distances less than $h/3$, attractive for distances between $h/3$ and h and zero for distances larger than h. Apart from the effects of small density and configurational fluctuations in the interior of the fluids, the total particle-particle interaction force acting on the fluid particles is nonzero only near fluid surfaces, fluid-fluid interfaces, and fluid-solid interfaces (at the walls of the fracture). In the boundary region, this force acts in the direction of the density gradient, creating surface tension.

Another advantage of using particle-particle interactions is the ability to model a variety of wetting behaviors at the solid boundaries. This can be achieved by placing stationary particles (denoted by subscript b) in the vicinity of the boundaries and assigning different interaction strengths s_{wb} and s_{nb} to the interactions between the nonwetting, n, and wetting, w, fluid particles and the boundary (fracture wall) particles. The strength of the wetting is determined by the strength of the fluid-boundary particle interactions relative to the strength of the fluid-fluid interactions. The short-range repulsive part of $\mathbf{F}_{ij}$, for the fluid-boundary interparticle interactions, also simulates no-flow boundary conditions in a manner similar to that employed by Monaghan [15], who used the repulsive part of a Lennard-Jones interaction between the boundary and fluid particles. The boundary particles are fixed in a narrow zone surrounding the nominal solid surface. Occasionally fluid particles will overcome the repulsive interactions with the boundary particles, and these particles are prevented from penetrating the fracture walls by using bounce-back boundary conditions at the nominal solid surface.

At each time step, the densities at each of the particles are calculated using Eq. (7), the pressure at each particle is obtained from the equation of state (12), and the acceleration of each fluid particle, $\mathbf{a}_i = d\mathbf{v}_i/dt$, was calculated from Eq. (13). The new particle position was calculated using the "velocity Verlet" algorithm [22], which takes the form

$$\mathbf{r}_i(t + \Delta t) = \mathbf{r}_i(t) + \Delta t \mathbf{v}_i(t) + 0.5\Delta t^2 \mathbf{a}_i(t) \quad (16)$$

and

$$\mathbf{v}_i(t + \Delta t) = \mathbf{v}_i(t) + 0.5\Delta t \{\mathbf{a}_i(t) + \mathbf{a}_i(t + \Delta t)\}. \quad (17)$$

To obtain a stable solution the time step Δt should satisfy the conditions $\Delta t \leq 0.25 h/3c$, $\Delta t \leq 0.25\min(h/3|\mathbf{a}_i|)^{1/2}$, and $\Delta t \leq \min(\rho_i h^2/9\mu_i)$, where $|\mathbf{a}_i|$ is the magnitude of the acceleration $\mathbf{a}_i$ [9].

A linked-list approach with an underlying square lattice (with the size of the lattice unit equal to the range of the weighting function, h, for computational efficiency) was used to rapidly locate all of the particles within a range h of any selected particle.

The dimensionless values of the constants used in the van der Waals equation of state were $kT = 0.1$, $\bar{c}_1 = 0.022$, and $\bar{c}_2 = 0.013$, and the dimensionless masses of the particles were set to unity.

III. SURFACE TENSION AND CONTACT ANGLES

In the modified SPH model, the surface tension and contact angles are not prescribed explicitly. Instead, they are determined by the interaction forces and the equation of state, and they must be determined from numerical experiments. To calculate the surface tension and verify the consistency of our model, four different numerical experiments were conducted: (i) small-amplitude shape fluctuations of a liquid drop, (ii) measurement of the pressure in the SPH liquid as a function of drop radius, (iii) capillary rise of fluid in a small aperture, and (iv) gravity-driven flow of droplets between two parallel walls.
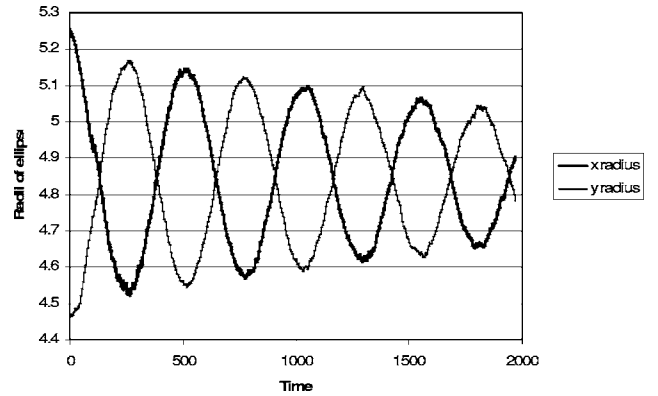

FIG. 1. Oscillations of a liquid drop initially deformed into an ellipse. Change of radii (in units of h) of the ellipse in the x and y directions with dimensionless time.

In the first numerical experiment, the small-amplitude fluctuations of two-dimensional liquid drop were studied. The surface tension σ can be found from the period of oscillations, τ, using the expression

$$\tau = 2\pi\sqrt{\frac{R^3\rho}{6\sigma}}, \quad (18)$$

given by Nugent and Posch [20], where R is the equilibrium radius of the drop and ρ is the density of the fluid in the drop. A two-dimensional drop was prepared by placing particles randomly inside a circle with a radius of 5 in units of h (the range of the weighting function), and the system was given time to reach equilibrium by running the SPH simulation with $\mathbf{g} = 0$. In the absence of gravity, the shape of the drop relaxes to a circle under the influence of the surface tension. At equilibrium, the radius of the drop, R, was found to be 4.84 in units of h, and the average density $\langle\rho\rangle$ was 59.1. After the system reached equilibrium, the drop was deformed into an elliptic shape with an eccentricity of $e = 0.55$ employing an area-preserving and, hence, density-conserving transformation of the particle coordinates [20]:

$$\begin{pmatrix} x_i' \\ y_i' \end{pmatrix} = \sqrt{\frac{2}{\sin\phi}} r_i \begin{pmatrix} \sin(\phi/2)\sin u_i \\ \cos(\phi/2)\cos u_i \end{pmatrix}, \quad (19)$$

where $r = \sqrt{x_i^2 + y_i^2}$, $u_i = \arctan(x_i/y_i)$, and $\phi = e\pi$.

After deformation into an ellipse, the drop underwent oscillations. Figure 1 shows how the radii of the ellipse in the x and y directions change with time. The figure shows that the oscillation decays with a period of $\tau = 510$. Despite the zero dynamic viscosity in Eq. (11) used in this numerical experiment, the amplitude of the oscillations decreased due to the intrinsic viscosity that is inherent in particle systems [13,23]. From Eq. (18), the value of the surface tension was determined to be $\sigma = 0.17$.

The surface tension can be determined from the equilibrium radius of a liquid drop and the pressure in its interior, P_0, using the Young-Laplace equation [20]:

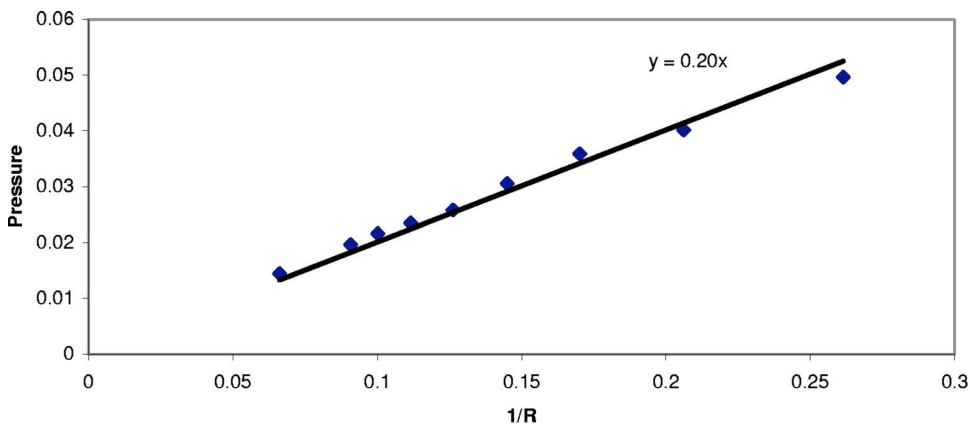$$P_0 = \frac{\sigma}{R}. \quad (20)$$

FIG. 2. (Color online) Dimensionless fluid pressure in the center of the liquid drop versus $1/R$ where R is a radius of the liquid droplet (in units of h).

Several liquid drops with radii ranging from 4 to 15 in units of h were created as described above. Figure 2 shows a plot of P_0 versus $1/R$, and a surface tension of approximately $\sigma = 0.2$ was obtained. Values of the surface tension obtained from drops of different sizes were quite consistent. The surface tensions of the smallest drops, with radii smaller than 5 (in units of h) were slightly smaller than 0.2. The Young-Laplace equation cannot be expected to hold when the drop is very small, and the surface width becomes comparable with the drop radius. In addition, the uncertainties in the estimated drop radius become larger relative to the radius when the radius is not much larger than the particle size and width of the surface.

Because of the particle-particle interactions $\mathbf{F}_{ij}$, the pressure inside the droplet cannot be obtained directly from the equation of state. However, Hoover [24] has shown that SPH is isomorphic with molecular dynamics with many-body particle-particle interactions. This allows the SPH equations and the particle-particle interactions to be treated in a consistent manner so that the pressure can be calculated from the *total* particle-particle interaction forces [22]:

$$P = P_k + \frac{1}{4\pi r^2}\sum_i \sum_j \mathbf{r}_{ij} \cdot \mathbf{f}_{ij}, \tag{21}$$

where P_k is the ideal gas (kinetic) contribution to the pressure and r is the "virial" radius of a circle in the middle of

liquid drop. The viscous forces are not compensated by random forces (as they would be in dissipative particle dynamics or Brownian dynamics simulations), and the essentially random relative motion of the particles generated by the nonequilibrium initial positions of the particles is quickly damped, leading to an effective kinetic temperature T that approaches zero as the drop approaches its equilibrium shape and surface energy is no longer being converted into kinetic energy. In the case of a drop at equilibrium, the particles are not moving. Consequently the ideal gas pressure P_k is zero. For the same reason, the viscous forces are zero and the interactions forces reduce to

$$\mathbf{f}_{ij} = -m_i m_j \left(\frac{P_j}{\rho_j^2} + \frac{P_i}{\rho_i^2} \right) \nabla_i W(\mathbf{r}_i - \mathbf{r}_j, h) + \mathbf{F}_{ij}. \tag{22}$$

The summation in Eq. (21) is over all i particles that lie inside the virial radius r and all j particles in the drop, and self-interactions ($i=j$) are excluded.

Figure 3 shows how the value of the pressure P_0 depends on the virial radius r for different droplet sizes. It can be seen that expression (21) gives consistent values for the pressure as long as r is less than approximately $R-1$, which suggest that the width of the surface is on the order of h. In Fig. 2 we used values of P_0 averaged over $r<R-1$.

In the third experiment, the capillary rise between two flat parallel walls (Fig. 4) that were inserted into a fluid layer
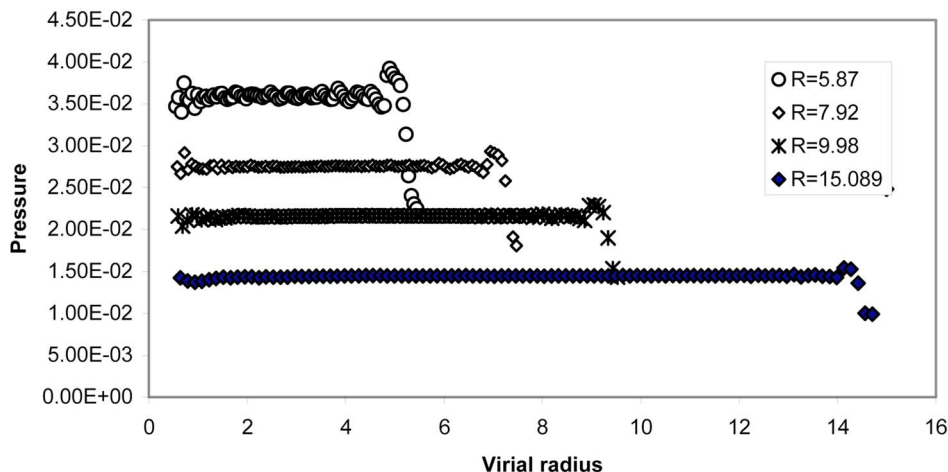

FIG. 3. (Color online) Dimensionless fluid pressure in center of the liquid drop versus virial radius r (in units of h) as a function of the radius of the liquid drop R (in units of h).
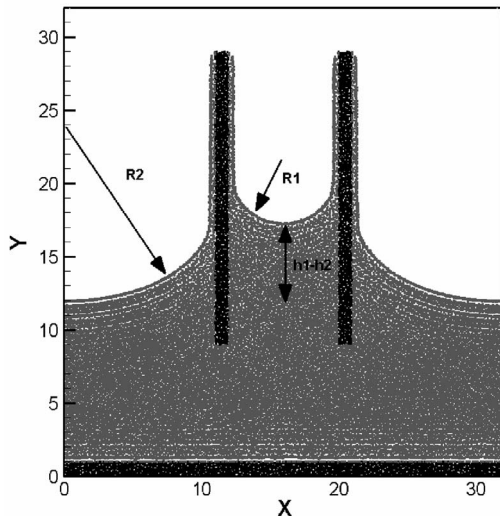
FIG. 4. Capillary rise between two parallel plates inserted into a fluid layer supported by an impermeable boundary. The flow domain is periodic in the horizontal direction. Black and gray particles denote the impermeable solid boundaries and the fluid. Size of flow domain is in units of h.
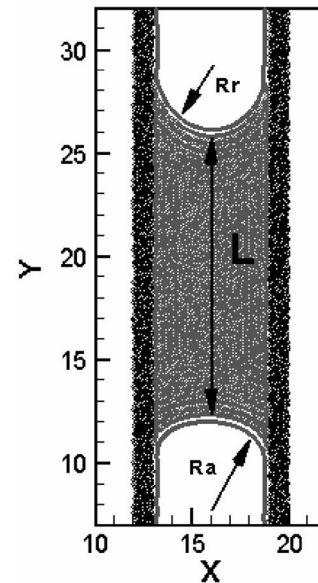

FIG. 5. Steady-state motion of a droplet between two parallel plates. Black and gray particles define the impermeable solid boundaries and fluid. Size of flow domain is in units of h.

supported by an impermeable lower boundary was simulated. To start the simulation, particles were placed randomly into a 32×32 box (in units of h) with periodic boundary conditions, and the evolution of the particles was simulated using Eq. (13). After the system reached equilibrium, the particles near the bottom of the model were "frozen" to form an impermeable lower boundary. The particles in two vertical layers near the middle were also frozen, as shown in the figure, to represent the walls. Then the remaining "mobile" particles above $y = 16$ were removed, and the flow simulation was started by applying a dimensionless gravitational acceleration of $g = 0.0001$. Figure 4 shows the equilibrium state of the system. The radii of curvatures of the fluid surfaces between the vertical walls were determined to be $R_1 = 4.05$ and $R_2 = 13.92$, the difference in fluid levels $h_1 - h_2$ was determined to be 5.27, and the surface tension ($=0.178$) was calculated using the expression

$$\rho g(h_1 - h_2) = \sigma\left(\frac{1}{R_1} - \frac{1}{R_2}\right). \qquad (23)$$

In the fourth test, the movement of a droplet between two parallel plates was studied (Fig. 5). To start the simulation, particles were placed randomly into a 32×32 box. After the system reached equilibrium, all the particles were removed, except for the particles representing the walls of the fracture (the black particles in Fig. 5, with x coordinates in the ranges $12 < x < 13$ and $19 < x < 20$) and the particles representing the droplet (particles with coordinates in the range $13 < x < 19$ and $14 < y < 31$). The interaction strength between the fluid and boundary particles was set to 1.1 times the fluid-fluid particle interactions. Then the simulation was run with zero gravity to allow the fluid drop to reach an equilibrium shape. Gravity was then applied in the negative y direction. After a steady-state flow was reached, the average velocity $\mathbf{v}$

of the particles in the droplet, the radii of curvature of the receding and advancing interfaces R_r and R_a, and length of the droplet, L, in the y direction, were measured. The surface tension σ was then calculated from

$$\mathbf{v} = \frac{b^2}{12\mu}\left\{\rho g + \frac{\sigma}{L}\left(\frac{1}{R_a} - \frac{1}{R_r}\right)\right\}. \qquad (24)$$

Two simulations were run with gravitational accelerations of $g_1 = 0.0001$ and $g_2 = 0.0002$. The corresponding velocities were $\mathbf{v}_1 = 0.02$ and $\mathbf{v}_2 = 0.043$, and the receding and advancing radii of curvature were $R_{r1} = 2.59$ and $R_{r2} = 2.27$ for $g = 0.0001$ and $R_{a1} = 5.37$ and $R_{a2} = 12.84$ for $g = 0.0002$. The droplet length was $L = 14.1$, the particle density was $\rho = 58.8$ in both simulations, and the prescribed dynamic viscosity was $\mu = 0.5$. It follows from the first experiment that the intrinsic viscosity is significant in nonlaminar flows. On the other hand, SPH simulations of Couette flow, Poiseuille [9] flow, and flow in porous media [10] show that the effects of the intrinsic contribution to the viscosity are very small for laminar flows. The surface tensions estimated from these simulations using Eq. (24) with a dynamic viscosity of $\mu = 0.5$ (assuming a zero intrinsic contribution to the viscosity) were $\sigma_1 = 0.179$ and $\sigma_2 = 0.180$.

The last two simulations show that the advancing contact angle increases (the radius of curvature increases) and the receding angle decreases with increasing fluid velocity. This behavior is well known [25–27]. Theoretical models for the dynamics of driven interfaces in random systems [28–31], three-phase contact line dynamics [32–35], computer simulations [36–38] and experimental investigations [1,39,40] suggest that $\theta - \theta^+ \propto |V|^\beta$ for an advancing contact line and $\theta^- - \theta \propto |V|^\beta$ for a receding contact line, where V is the contact line velocity, θ^+ is the advancing contact angle, and θ^- is the receding contact angle.
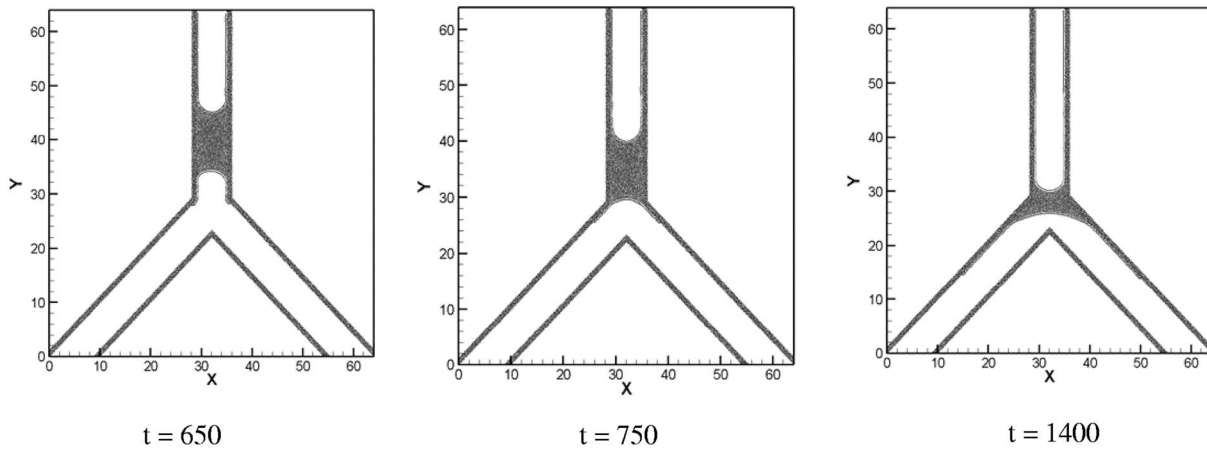
FIG. 6. Droplet flow through a Y-shaped fracture junction at three different times with a gravitational acceleration of $g=0.0001$. Black and gray particles denote the impermeable solid boundaries and the fluid. Size of flow domain is in units of h.

The values of the surfaces tension obtained from all four numerical experiments were in very good agreement. The consistency between the four independent numerical tests shows that the model used in this investigation can accurately simulate surface tension and fluid-solid interactions under both static and dynamic conditions.

IV. FLOW THROUGH FRACTURE JUNCTIONS

Next, flow through an inverted Y-shaped fracture junctions was simulated (Figs. 6–8). The initial setup for the simulation was similar to those used in the simulations described above. First, particles were randomly placed in a 64×64 box. After the system reached equilibrium, all of the particles were removed, except for particles representing the inverted Y-shaped walls of the fracture junction (the black particles on Figs. 6–8) and the gray particles representing the initial distribution of fluid (particles with coordinates $29 < x < 35$ and $43 < y < 61$). The positions of the boundary particles used to represent the fracture walls were kept fixed during the rest of the simulation, and the interaction strength

between fluid and boundary particles was set to 1.1 times the fluid-fluid particle interaction strength. Then the simulation was run with zero gravity to allow the fluid to reequilibrate. After the fluid had equilibrated and the curvatures of the fluid surfaces had reached their asymptotic (long time) values, gravity was applied in the negative y direction. Depending on the magnitude of the gravitational acceleration, or Bond number (Bo) three different types of behavior were observed at the intersection. The Bond number for our simulations can be defined as

$$Bo = \rho g L_1 L_2 / \sigma, \qquad (25)$$

where $\rho = 59$, the width of the fracture is $L_1 = 6$, the length of the droplet is $L_2 = 15$, and the average value of the surface tension from the four tests described above was $\sigma = 0.181$.

For $g = 0.0001$ (Bo$=2.92$) (Fig. 6) the droplet stopped at the intersection, and flow continued in the form of films on the outer walls of the fractures.

When the gravitational force was increased to $g = 0.000\,11$ (the Bond number was increased to 3.21) (Fig. 7), film flow still occurred but the droplet was able to overcome
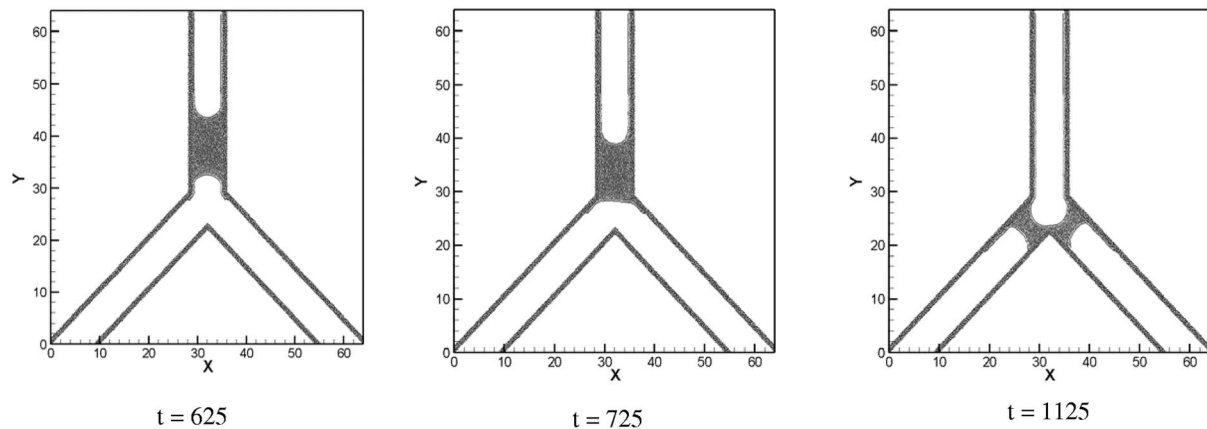

FIG. 7. Droplet flow through a Y-shaped fracture junction at three different times with a gravitational acceleration of $g=0.00011$. Black and gray particles define the impermeable solid boundaries and the fluid. Size of flow domain is in units of h.
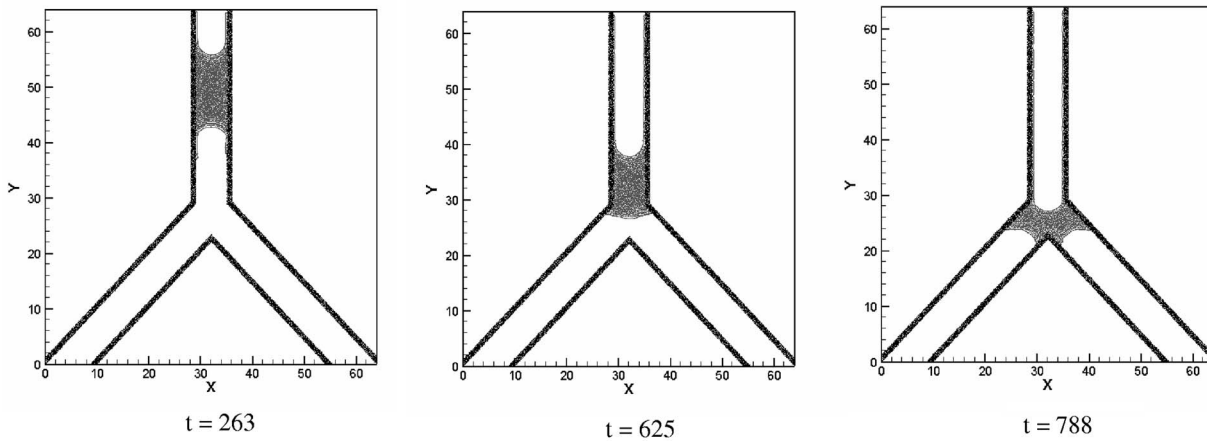
FIG. 8. Droplet flow through a Y-shaped fracture junction at three different times with a gravitational acceleration of $g=0.00015$. Black and gray particles define the impermeable solid boundaries and the fluid. Size of flow domain is in units of h.

the capillary barrier and enter the intersection. A further increase in the gravitational acceleration to $g=0.000\,15$ (Bo $=4.38$) allowed the fluid to overcome the capillary barrier relatively rapidly and fill the intersection without film development, as Fig. 8 illustrates. Figure 9 shows sketches of the experimental results taken from Dragila and Weisbrod [1]. In their experiments, Dragila and Weisbrod used droplets of different sizes to change the effect of gravity acting on the fluid, while in our simulations the acceleration due to gravity was changed to achieve a similar effect in terms of Bond numbers. Dragila and Weisbrod [1] found that for small Bond numbers Bo<2.059 (droplets shorter than 1 cm), the droplet stops at the intersection and flow continues in the form of film flow. For intermediate Bond numbers $2.059<$Bo <3.089 (droplets between 1 cm and 1.5 cm), the droplets slow down and film flow occurs, but the intersection is eventually saturated. Finally, for large Bond numbers $3.089 <$Bo (droplets large than 1.5 cm), droplets saturate the intersection and film flow does not occur. Dragila and Weisbrod [1] did not report the Bond numbers in their experiments, so we estimated the Bond numbers assuming that the density of water, ρ, is 998.2 kg/m^3 and the water-air surface tension σ is 0.076 N/m. Figures 6–8 show that the simulations captured all the essential elements of the experimental results shown in Fig. 9, such as the formation of capillary bridges accompanied by film flow for small Bond numbers (Fig. 6) and the flow of droplets that overcome the capillary barrier, with preceding film flow for intermediate Bond numbers (Fig. 7) and without film flow for large Bond numbers (Fig. 8). We attribute the small quantitative inconsistency in droplet behavior as a function of Bond number between the experiments and numerical simulation to several factors including uncertainties in the contact angle and wetting behavior in both the simulations and experiments, three-dimensional effects in the experiments that are not captured in the two-dimensional simulations, insufficient numerical resolution in the simulations, and experimental uncertainties such as uncertainties in estimating the droplet heights [Dragila and Weisbrod gave only approximate drop heights (1.0 and 1.5 cm) at the transitions between different behaviors]. The behavior of the thin films in the experiments depends on

physical processes occurring over a very wide range of length scales (from molecular or near-molecular scales near the three-phase contact lines and the fluid-solid interfaces to hydrodynamics on the macroscopic scale of the film thickness). In contrast to this, the thickness of the film in the SPH simulations is smaller than the range of the weighting function. The SPH simulations could be improved by increasing the resolution of the simulations. However, this would require a large increase in computer resources, and the full range of length scales that are important in film flow would still be far out of reach. One possible solution would be to use adaptive particle splitting and coalescence methods that would allow smaller particles to be used near the solid boundaries and larger particles to to be used to simulate bulk fluid flow. An alternative would be to use hybrid models combining molecular dynamics or dissipative particle dynamics to simulate molecular-scale and -mesoscale processes with SPH to simulate larger-scale hydrodynamic processes.
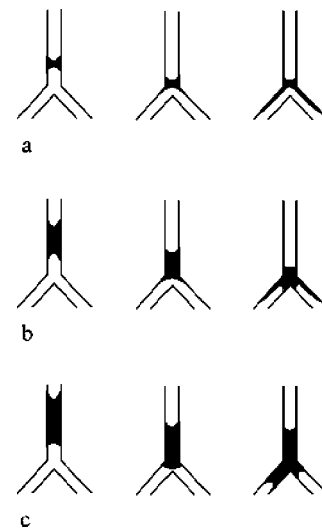

FIG. 9. Spatial distribution of water in a Y-shaped fracture junction. The solid regions are fluid filled. Time progresses from left to right. (a) Droplets shorter than 1.0 cm. (b) Droplets between 1.0 and 1.5 cm. (c) Droplets longer than 1.5 cm (after Dragila and Weisbrod [1], published with permission of the authors).

V. DISCUSSION AND CONCLUSIONS

A combination of standard SPH equations with particle-particle interactions was used to simulate partially saturated fluid flow in fracture junctions. The consistency of the surface tension values obtained from four independent numerical tests demonstrated that the modified SPH model could accurately represent the effects of surface tension and fluid-solid interactions. The results of numerical simulations of flow through fracture intersections were in qualitative agreement with laboratory experiments. Although the simulations lead to film flow that resembles that seen in the experiments, the implications of this apparent agreement should be treated cautiously due to the limited resolution of the numerical simulations.

We attribute the realistic contact-line dynamics to the interactions between the fluid particle and the randomly distributed boundary particles representing the fracture walls. The motion of the contact line is controlled by the interplay between the random pinning forces created by these interactions and the driving force resulting from the effects of gravity acting on the fluid phase. These are the key ingredients of some of the models that have been proposed for contact line dynamics [28–31]. However, the dynamics of the contact points in two-dimensional simulations cannot be expected to be quantitatively similar to the behavior of the contact line in three-dimensional systems.

ACKNOWLEDGMENTS

[1] M. I. Dragila and N. Weisbrod, Water Resour. Res. **40**, W02403 (2004).

[2] M. Pooladi-Darvish and A. Firoozabadi, J. Can. Petr. Technol. **39**, 31 (2000).

[3] G. I. Tripp and J. R. Vearncombe, J. Struct. Geol. **26**, 1087 (2004).

[4] A. A. Keller, M. J. Blunt, and P. V. Roberts, Transp. Porous Media **38**, 189 (2000).

[5] P. Yue, J. J. Feng, C. Liu, and J. Shen, J. Fluid Mech. **515**, 293 (2004).

[6] D. Rothman and S. Zaleski, *Lattice-Gas Cellular Automata* (Cambridge University Press, Cambridge, England, 1997).

[7] S. Succi, *The Lattice Boltzmann Equation for Fluid Dynamics and Beyond* (Oxford Science, Oxford, 2001).

[8] W. R. Osborn, E. Orlandini, M. R. Swift, Y. M. Yeomans, and J. R. Banavar, Phys. Rev. Lett. **75**, 4031 (1995).

[9] G. Gonnella, E. Orlandini, and J. M. Yeomans, Phys. Rev. E **58**, 480 (1998).

[10] X. Shan and H. Chen, Phys. Rev. E **47**, 1815 (1993).

[11] J. Hoogerbrugge and J. M. V. A. Koelman, Europhys. Lett. **19**, 155 (1992).

[12] P. Español and P. Warren, Europhys. Lett. **30**, 191 (1995).

[13] L. B. Lucy, Astron. J. **82**, 1013 (1977).

[14] R. A. Gingold and J. J. Monaghan, Mon. Not. R. Astron. Soc. **181**, 375 (1977).

[15] J. J. Monaghan, J. Comput. Phys. **110**, 399 (1994).

[16] J. P. Morris, P. J. Fox, and Y. Zhu, J. Comput. Phys. **136**, 214 (1997).

[17] Y. Zhu, P. J. Fox, and J. P. Morris, Int. J. Numer. Analyt. Meth. Geomech. **23**, 881 (1999).

[18] Y. Zhu and P. J. Fox, Transp. Porous Media **43**, 441 (2001).

[19] J. P. Morris, Int. J. Numer. Methods Fluids **33**, 333 (2000).

[20] S. Nugent and H. A. Posch, Phys. Rev. E **62**, 4968 (2000).

[21] J. J. Monaghan, Annu. Rev. Astron. Astrophys. **30**, 543 (1992).

[22] M. P. Allen and D. J. Tildesley, *Computer Simulation of Liquids* (Oxford University Press, Oxford, (2001), p. 81.

[23] H. A. Posch, W. G. Hoover, and O. Kum, Phys. Rev. E **52**, 1711 (1995).

[24] W. G. Hoover, Physica A **260**, 244 (1998).

[25] R. H. Dettre and R. E. Johnson, J. Phys. Chem. **69**, 1507 (1965).

[26] R. E. Johnson and R. H. Dettre, J. Phys. Chem. **68**, 1744 (1964).

[27] P. G. de Gennes, Rev. Mod. Phys. **57**, 827 (1985).

[28] O. Narayan and D. S. Fisher, Phys. Rev. B **48**, 7030 (1993).

[29] T. Nattermann, S. Stepanow, L. H. Tang, and H. Leschhorn, J. Phys. II **2**, 1483 (1992).

[30] J. Koplik and H. Levine, Phys. Rev. B **32**, 280 (1985).

[31] D. Ertas and M. Kardar, Phys. Rev. E **48**, 1228 (1993).

[32] E. Raphael and P. G. Degennes, J. Chem. Phys. **90**, 7577 (1989).

[33] R. G. Cox, J. Fluid Mech. **168**, 195 (1986).

[34] T. E. Mumley, C. J. Radke, and M. C. Williams, J. Colloid Interface Sci. **109**, 398 (1986).

[35] R. L. Hoffman, J. Rheol. **26**, 606 (1982).

[36] J. F. Joanny and M. O. Robbins, J. Chem. Phys. **92**, 3206 (1990).

[37] P. Raiskinmaki, A. Shakib-Manesh, A. Jasberg, A. Koponen, J. Merikoski, and J. Timonen, J. Stat. Phys. **107**, 143 (2002).

[38] L. W. Fan, H. P. Fang, and Z. F. Lin, Phys. Rev. E **63**, 051603 (2001).

[39] L. H. Tanner, J. Phys. D **12**, 1473 (1979).

[40] E. Schaffer and P.-Z. Wong, Phys. Rev. E **61**, 5257 (2000).